



Degassing of a pressurized liquid saturated with dissolved gas when injected to a low pressure liquid pool

Ourania Oikonomidou, Sotiris P. Evgenidis, Margaritis Kostoglou, Thodoris D. Karapantsios*

Division of Chemical Technology, School of Chemistry, Aristotle University of Thessaloniki, University Box 116, 541 24 Thessaloniki, Greece

ARTICLE INFO

Keywords:

Gas desorption
Decompression
Nozzle
Dissolved air flotation
Bubble size distribution
Gas fraction

ABSTRACT

Bubbles forming due to decompression of a liquid saturated with dissolved gas at elevated pressures when it enters a low pressure liquid pool can either limit or promote the efficiency of several ground and space applications. Among the experimental parameters influencing flow decompression degassing, dissolution pressure is the most studied, yet controversial, parameter. The present work aims to shed light on how dissolution pressure of a liquid affects the final size of bubbles and the generated gas fraction by conducting gas desorption (degassing) experiments of liquid jets that decompress passing through a nozzle to a vertical column filled with the same non-degassed liquid. Bubbles size distributions at different radial positions in the column are computed analyzing high resolution digital images. A patented electrical impedance technique is employed to measure instantaneously local volumetric gas fraction. Flow dispersion in the column is studied by residence time distributions using conductivity tracers. On-line continuous dissolved oxygen measurements yield the kinetics and final extent of degassing. Experimental results are discussed to comprehend why bubbles size distributions vary with dissolution pressures and how this variation affects gas fraction in the column.

1. Introduction

The formation of bubbles during decompression of a liquid saturated with dissolved gas is caused by desorption of the dissolved gas. The extent of gas desorption depends on the level of supersaturation. Therefore, when a saturated liquid is decompressed, dissolved gas desorbs until the liquid reaches equilibrium again regarding the final pressure conditions [1]. Bubble formation during liquid degassing may be also initiated by cavitation in case pressure drops below the vapor pressure [2–4]. The generated bubbles grow in size due to mass transfer, until the gas concentration gradient between bubbles and surrounding liquid becomes zero [5,6]. Even after the completion of liquid degassing, bubble size may further evolve due to coalescence of adjacent bubbles [7].

Flow decompression degassing is the process which a pressurized saturated liquid undergoes when its pressure drops, e.g. when it exits a nozzle or an orifice. It is encountered in a number of ground and space applications. In some applications, the formation of bubbles due to flow decompression degassing is undesirable. For instance, degassing of liquids in miniature loop heat pipes (mLHPs), used for thermal control of electronics in workstations and satellites, limit their heat removal capacities [8]. Similarly, decompression degassing of lubricants while

circulating in aircraft turbines deteriorates their cooling properties [9]. In industry, cavitation may cause the aging of pumps [10]. In oil recovery, water must be de-oxygenated prior to injection, as the desorption of oxygen promotes corrosion and growth of certain bacteria [11]. Furthermore, Decompression Sickness (DCS) is triggered by the formation of bubbles desorbing from the supersaturated body tissues of divers and astronauts, when they are exposed to reduced pressure conditions [12]. On the contrary, there are applications where flow decompression degassing is desirable. For instance, it constitutes the main working principle of Dissolved Air Flotation (DAF) in wastewater treatment applications. In DAF tanks, water saturated with dissolved air is injected through nozzles to generate bubbles that adhere onto suspended solid particles and promote their separation from wastewater by dragging them to the tank free surface [13]. Regarding space, the injection of a liquid propellant containing dissolved gases inside the combustion chamber of a rocket, may improve spray atomization [14].

The size of bubbles is a crucial parameter for the applications' efficiency and proper functioning. In order to be able to control the size of generated bubbles in flow decompression degassing systems, it is important to study the effect of several experimental parameters on final bubble size. In literature, such works were conducted chiefly with respect to DAF application. Researchers have studied the influence of

* Corresponding author.

E-mail addresses: oikonomid@chem.auth.gr (O. Oikonomidou), sevgenid@chem.auth.gr (S.P. Evgenidis), kostoglu@chem.auth.gr (M. Kostoglou), karapant@chem.auth.gr (T.D. Karapantsios).

<https://doi.org/10.1016/j.exptthermflusci.2018.03.018>

Received 23 October 2017; Received in revised form 23 February 2018; Accepted 18 March 2018

Available online 19 March 2018

0894-1777/ © 2018 Elsevier Inc. All rights reserved.

Nomenclature

C	dissolved gas concentration (kg/m ³)
C _{eq}	gas solubility (kg/m ³)
D	column internal diameter (m)
d _{1,0}	mean bubble diameter (m)
F _m	Foaming number (-)
L	column height (m)
L ₁	height of perfect mixing in the column (m)
Q	liquid flow rate (m ³ /s)
R	column radius (m)
R _c	bubble critical radius (m)
r	radial distance from the column center (m)
Re _{flow}	flow Reynolds number (-)
Re _{jet}	jet Reynolds number (-)

S	supersaturation (-)
StDev	gas fraction standard deviation (-)
t	time during injection (s)
t _{residence}	jet average residence time in the column (s)
t ₁	jet residence time in the mixing zone (s)
t ₂	jet residence time in the plug flow (s)
U _{bubbles}	bubble velocity (m/s)
U _{buoyancy}	bubble velocity due to buoyancy (m/s)
U _{flow}	flow velocity in the column (m/s)
U _{jet}	jet velocity (m/s)
V	volume of the column (m ³)
z	vertical distance from column's bottom (m)
γ	surface tension (N/m)
ε	gas fraction (-)
σ	bubble diameter standard deviation (-)

several DAF experimental parameters on the size of bubbles, motivated by the fact that the large surface area provided by microbubbles amplifies the possibility of bubble-floc successful collision [15,16]. Namely, Rykaart and Haarhoff [7], Takahashi et al. [17], Ponasse et al. [18] and De Rijk et al. [19], have studied the effect of nozzle geometry on bubble size. The role of liquid surface tension [18,20], liquid viscosity [21,22] and gas solubility [16] and have been investigated as well. Other examined parameters are the liquid flow rate [17,19], partial liquid saturation [3,16], turbulence intensity in the saturation system [23] and the introduction of extra air at the nozzle's top to break the bubbles [24].

Nevertheless, the most studied experimental parameter of all is the pressure level at which liquid is saturated with the gas (dissolution pressure), as it determines the concentration of dissolved gas in the liquid mass. Yet, the effect of dissolution pressure on bubble size remains controversial. Some researchers report experimental results that

indicate generation of smaller bubbles when higher dissolution pressures are employed [13,16,17,19]. Contrarily, some others report that dissolution pressure does not affect bubble size at all [7,23,25]. Rodrigues and Rubio [25] state that bubble size is exclusively associated with the type of nozzle and that employment of higher dissolution pressures results only in higher populations of same sized bubbles, due to the higher concentrations of dissolved air. In between, there are researchers supporting that there is a maximum dissolution pressure above which there is no significant effect on bubble size. For water as the injected liquid, Couto et al. [20] spot this critical maximum pressure at 300 kPa, while Schers and Van Dijk [26] at 500 kPa. Comparison between the average bubble sizes obtained from the above studies is meaningless due to varying experimental conditions (nozzle geometry, column dimensions, mixing). Moreover, macrobubbles present in the corresponding two phase flows are either taken [7,18,20] or not taken [19,25] into consideration during measurements.

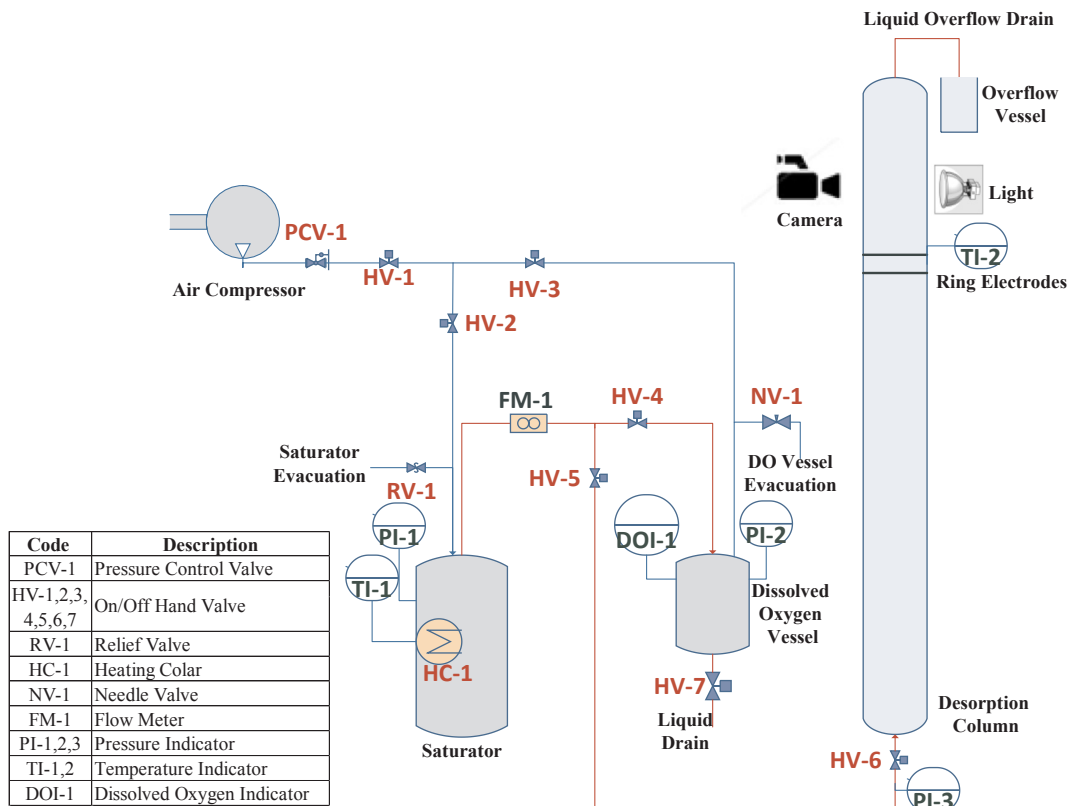


Fig. 1. Flow diagram.

The above controversy is the motivation for this work. On this account, flow decompression degassing experiments are carefully designed and executed. For the first time, the effect of dissolution pressure on final bubble size is studied combining measurements of a number of experimental quantities: size distribution of bubbles at different radial positions in the column, local instantaneous volumetric gas fraction, flow dispersion (liquid jet-bulk mixing) in the column, kinetics and final extent of gas desorption. The experimental results are discussed in detail, aiming to correlate them with bubbles formation, growth and dispersion along the column.

2. Materials and methods

The experimental setup is shown in a flow diagram, Fig. 1. The gas phase dissolves and saturates the liquid phase inside the saturator. The saturator is a stainless steel pressure resistant cylindrical vessel. Liquid phase is manually introduced in the saturator through a removable lid until it is approximately half full. High pressure gas generated by a compressor enters the saturator through flexible tubes. Desired pressure levels are regulated by a pressure control valve (PCV-1). Pressure conditions inside the saturator are indicated by a pressure gauge (PI-1). Saturation of the liquid phase with gas is achieved by vigorous manual shaking of the vessel which rapidly refreshes large surface areas for mass transfer. Shaking is continuous until the vessel pressure stabilizes to a desired dissolution pressure (above ambient pressure) which means that gas dissolution has approximately reached equilibrium at this pressure.

The level of liquid saturation (%) is measured before each experiment. A special sealed stainless steel cylindrical vessel (Dissolved Oxygen Vessel) is constructed for this purpose. The gas saturated liquid is transferred from the saturator to the DO vessel by means of a small pressure difference (a slight opening of HV-7 generates 10 kPa pressure difference between the two vessels). A dissolved oxygen optical probe (Pro ODO, YSI) is fixed air-tight in the DO vessel (DOI-1). This probe is tolerant to pressure exposure up to 600 kPa.

Decompression experiments take place in a plexiglass vertical column, open to atmosphere. The column is 147 cm long with internal diameter $D = 40$ mm. The column is filled with test liquid up to its top. An aluminum nozzle with a 600 μm diameter is adjusted at the bottom of the column through which saturated liquid is injected upwards inside the column. Nozzle geometry is presented in Fig. 2. This vertical injection allows the jet to travel enough distance without interference with the column walls. Upon its exit from the nozzle, the liquid jet is exposed to ambient pressure (plus a hydrostatic pressure of 147 cm water) and becomes supersaturated with dissolved gas. Instantly, gas desorption starts. Gas bubbles nucleate within the liquid jet and grow in size while ascending in the column towards the liquid free surface. In order to maintain the same conditions during the whole experiment, the level of decompression has to remain constant. To do so, compressed air keeps entering the saturator at the desired pressure level during the whole injection period. The flow rate of the saturated liquid injected in the column is measured by a turbine flow meter (FHK-Ryton-10, GREISINGER) (FM-1). During the injection, the column overflows and the overflowing liquid is collected inside an open vessel through a tubing system. As a result, the column height and thus the hydrostatic pressure remains constant during the experiment.

In case the liquid pressure drops below vapor pressure at the constriction part of the nozzle, cavitation occurs and vapor bubbles form inside the nozzle. However, pressure recovery at the nozzle exit forces the generated vapor to recondense instantaneously. The remaining bubble nuclei act together with other microparticles present in the liquid phase (e.g. liquid pollutants), as nucleation sites for liquid degassing (dissolved gas transfers from the supersaturated liquid mass to the bubble nuclei growing their size) [3]. Therefore, the possibility of cavitation is expected to affect the number and size of degassing bubbles to some extent, however this effect is difficult to be quantified.

Experiments are performed at 25 °C. A bath circulator (C10, Thermo Haake) is used to thermal regulate the liquid phase before it is introduced to the saturator and the column. The gas-liquid system under investigation is atmospheric air and NaCl solution (0.019% w/w) in deionized water. Electrical conductivity of the liquid phase is 500 $\mu\text{S}/\text{cm}$, simulating that of tap water. Dissolution pressure is the main experimental variable. Four different saturation (absolute) pressure levels are examined (220 kPa, 300 kPa, 400 kPa and 500 kPa). Table 1 presents the experimental conditions for each dissolution pressure. The measured liquid flow rate (Q) values fit with Bernoulli equation in case of a $0.8 (\pm 0.03)$ discharge coefficient. Jet velocity (U_{jet}) at the nozzle exit equals the measured liquid flow rate over the nozzle cross-sectional area. Similarly, liquid flow velocity in the column (U_{flow}) is calculated considering the measured liquid flow rate and the column cross-sectional area. Jet and liquid flow Reynolds numbers (Re_{jet} , Re_{flow}) are also shown indicating the corresponding turbulence intensities. The flow is highly turbulent in the jet region but laminar away from the jet.

It is noted that the present experimental campaign refers to the combined variation of dissolved gas concentration and liquid jet flow rate (as occurs in real decompression liquid degassing applications). The goal of this work is to obtain an overview of the dominant phenomena of the process. At a next step the important experimental parameters will be isolated in order to evaluate their separate contribution to the process outcome (e.g. bubble size distribution).

Bubbles images are recorded using a still digital camera (CANON EOS 70D) with a frame resolution of 20MP, supported by CANON EF 100 mm f/2.8 Macro USM Lens and six CANON extension rings (total length 130 mm) for magnification. The camera is fixed on a micrometering translation table to enable focusing on specified radial positions across the column. A cool white LED spot is adjusted as backlight diametrically opposite to the camera to illuminate the flow inside the column (Fig. 3a). Optical measurements are conducted 90 cm above the nozzle exit ($z/D = 22.5$). The decision to measure at this height is justified later in the text. Bubble images are captured at different radial positions across the column. These positions are: the region close to column walls ($r/R = 1$), 5 mm away from the column walls ($r/R = 0.75$) and 15 mm away from the column walls ($r/R = 0.25$), where “ r ” is the distance from the center of the column and “ R ” is the column radius. Focus at $r/R = 0.25$ is possible only in case of dilute bubbly flow (220 kPa). Optical distortion due to the cylindrical shape of the column is estimated by capturing images of a mesh, immersed at different radial positions inside the column. According to the results, vertical mesh

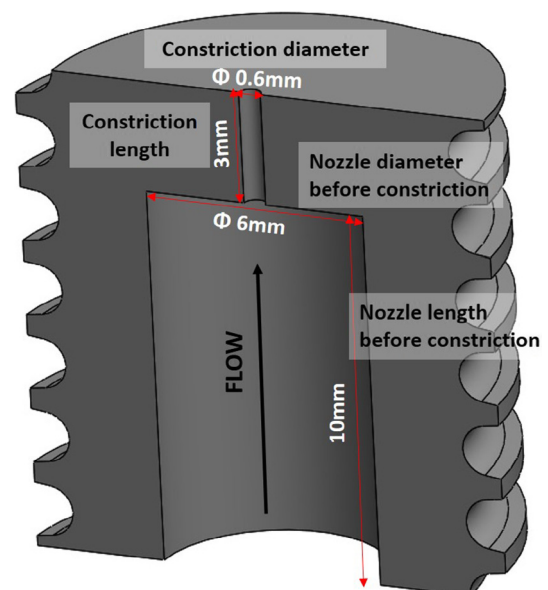


Fig. 2. Nozzle geometry schematic description (cut view).

Table 1
Experimental conditions under the working dissolution pressures.

	Q (L/min)	U_{jet} (m/s)	Re_{jet} (-)	U_{flow} (mm/s)	Re_{flow} (-)
220 kPa	0.191	11.3	6759	2.5	101
300 kPa	0.281	16.6	9943	3.7	149
400 kPa	0.325	19.2	11,500	4.3	173
500 kPa	0.368	21.7	13,022	4.9	195

dimension remains unaffected both by the column shape and the radial distance. Thus, determination of bubble size is based on their ‘vertical radius’. A shutter speed of 1/1250, an f-number varying from f/11 to f/16 and an ISO number of 1000 are the camera settings applied for capturing proper bubble images. The depth of field is $\Delta r/R = 0.05$ and the optical resolution is 3 pixel/4 μm . To check for repeatability, experiments are conducted three times per experimental condition (dissolution pressure and radial position).

CANON EOS Utility software is used to capture bubble images automatically every 5 s. Obtained data are saved as raw images and are imported to a custom software [27] for analysis. This software is capable of bubbles auto-detection and radius measurement, resulting in Bubble Size Distributions (BSD). More than 500 bubbles are measured at each experimental run in order to obtain statistically significant results. Arithmetic mean bubble diameter $d_{1,0}$ and standard deviation σ are calculated for single peak BSDs. For bimodal BSDs, in addition to the overall $d_{1,0}$, also the mean diameter $d_{1,0}$ and standard deviation σ of each peak are calculated.

Volumetric gas fraction measurements are conducted simultaneously with optical measurements using a patented ultra-sensitive electrical impedance technique [28]. The technique senses the flow using a pair of metallic ring electrodes located at 90 cm above the nozzle exit ($z/D = 22.5$), flush-mounted at the inner walls of the column (Fig. 3b). The distance between the two electrodes is $\Delta z/D = 0.5$, so the measuring volume is 25 ml. Continuous electrical impedance data obtained during measurement are transformed into gas fraction time series based on Maxwell’s model. Further information regarding the technique is provided by Evgenidis and Karapantsios [29].

Residence time distributions are estimated using conductivity tracers (NaCl), aiming to study mixing conditions inside the column when a liquid jet discharges from the nozzle into the liquid in the column at various dissolution pressures. A compressed aqueous NaCl solution of high conductivity (1000 $\mu\text{m}/\text{S}$) (not gas saturated) is injected into deionized water contained in the column. The overflowing liquid from the column enters a 250 ml open vessel (Overflow Vessel, Fig. 1). A digital electrical conductivity probe (HI763100, Hanna Instruments) is immersed in the vessel, providing instantaneous measurements of liquid overflow electrical conductivity. Experiments are also conducted to examine whether the presence of bubbles modify the mixing profile in the column. For this, the compressed liquid is first saturated with

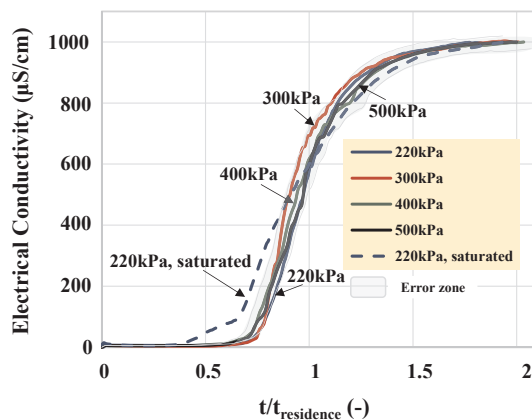


Fig. 4. Non saturated and saturated residence time distributions using conductivity tracers under various initial pressures.

dissolved gas before injection, so as its decompression to provoke bubble formation in the column.

Aiming to verify that bubbles have gained their final size when reaching the measuring point ($z/D = 22.5$), gas desorption kinetics and final extent of degassing are evaluated. For this purpose, decompression degassing experiments under various dissolution pressures are conducted, during which the remaining dissolved oxygen concentration is measured in the liquid as it overflows from the column at $z/D = 22.5$. The DO optical probe is immersed in the Overflow Vessel, yielding continuous dissolved oxygen readings during the experiments.

3. Results

3.1. Flow dispersion

The evolution of Electrical Conductivity (EC) tracer concentration in the absence of bubbles is presented in Fig. 4. In order to directly compare these residence time distribution curves, they are plotted versus reduced time, i.e., EC ($t/t_{residence}$). This is accomplished by dividing real time values with the liquid jet’s residence time inside the column. The average residence time in the column $t_{residence}$ equals the volume of the column (V) divided by the jet flow rate (Q). The maximum $t/t_{residence}$ value shows that the total volume of injected liquid equals two times the liquid volume in the column. However, the time required for the column to get completely filled with the incoming jet is less, $\sim 1.7 * t_{residence}$, as indicated by the moment the overflow electrical conductivity reaches a plateau. At the beginning of injection, $t/t_{residence} = 0$, the liquid overflow stream consists completely of deionized liquid preexisting in the column. Thus, electrical conductivity values are very low (0–20 $\mu\text{S}/\text{cm}$). Moreover, the zero slope of the curves denote a plug flow behavior. At some point the slope increases.



Fig. 3. (a) Camera and lighting during optical measurements, (b) Electrodes adjusted on the column during electrical measurements.

This abrupt increase is attributed to mixing of the incoming jet with the column liquid. The similarity among curves in Fig. 4 implies that the effect of dissolution pressure on flow dispersion inside the column is not significant. The slight deviation of the residence time distribution under 300 kPa from those under 220 kPa, 400 kPa, 500 kPa is considered within the margin of experimental error and has no direct physical meaning. Comparison between the solid line (unsaturated liquid) and the dashed line (saturated liquid) for 220 kPa in Fig. 4 illustrates the influence of bubbles formation on flow behavior. Bubbles generated due to decompression of saturated liquid shortens the initial (zero slope) plug flow period and amplify mixing. The presence of bubbles has two effects on residence time distributions. One is to reduce residence time (by increasing volumetric flow) and the other to increase dispersion (by creating liquid velocity profiles around the bubbles) [30]. These two effects explain the profile of residence time distribution in the presence of bubbles shown in Fig. 4. Curves for saturated liquid injection at other dissolution pressures show alike behavior, but are not displayed because of data overcrowding.

3.2. Gas desorption efficiency

The concentration of dissolved gas determining the liquid saturation state is proportional to pressure (Henry's law). Initial liquid saturation is a parameter regularly mentioned in studies regarding DAF efficiency, as it determines the liquid-bubble mass transfer gradient and thus affects both bubble growth rate and final bubble size. Interestingly, Vlyssides et al. [16] claimed that final bubble size is affected by the applied decompression step, ΔP , but is insensitive to whether the liquid is fully or partially saturated. In the present work the initial saturation of the compressed liquid is measured by the Dissolved Oxygen (DO) optical probe, prior to injection. According to DO measurements, compressed liquid is always $\sim 90\%$ saturated regardless of the duration of vigorous shaking of the saturator and the employed pressure. This value suggests satisfactory efficiency of the employed saturation system since saturation values reported in literature vary from 70 to 97% [13,16,19,24,31].

Fig. 5 shows the concentration of oxygen dissolved in the liquid stream overflowing from the column at $z/D = 22.5$ during the injection of a compressed, gas saturated, liquid jet inside the column. Different curves correspond to different initial pressures employed for liquid compression and saturation. At the beginning of all curves, dissolved oxygen is below the saturation level concerning atmospheric pressure and temperature of 25 °C (8.26 mg/L). This is not surprising, as at the beginning of injection the overflowing liquid is actually the liquid preexisting in the column. Small differences in the initial dissolved oxygen values between the curves correspond to different days of the experiments and thus different levels of saturation of the preexisting column liquid. Fig. 5 indicates that the injected liquid stream gets almost completely degassed when reaching $z/D = 22.5$. Even in the case of 500 kPa, where the liquid jet initial supersaturation is the highest (360% of the value at atmospheric pressure), liquid overflow supersaturation decreases to 13.5% (9.4 mg/L). This means that above $z/D = 22.5$, bubbles are not expected to grow further in size because the driving force for gas desorption diminishes. Consequently, one can assume that the optical and electrical results obtained at $z/D = 22.5$ correspond to almost completely degassed liquid.

3.3. Bubbles size distribution

First goal of the optical measurements is to investigate whether bubbles are homogeneously distributed across the column for every dissolution pressure. Indicative bubble images captured at $r/R = 1$, $r/R = 0.75$ and $r/R = 0.25$ are presented in Fig. 6 for all the examined dissolution pressures. In case of 220 kPa and 300 kPa, bubble images at different radial distances look alike. On the other hand, bubble radial distribution is not so homogenous for 400 kPa and 500 kPa, as the

fraction of large bubbles over small ones seems to increase when approaching the column center ($r/R = 0.75$) [32]. It must be noted that the boundaries of bubbles flowing close to the column center (at $r/R = 0.25$) are considered accurate only under the dissolution pressure of 220 kPa. This happens because the great population of intervening bubbles under 300 kPa and 400 kPa hide the bubbles flowing close to the center and result in blurry images. Image capturing at $r/R = 0.25$ under 500 kPa was not possible for technical reasons.

The visual observations above are further supported by Fig. 7. This Figure presents BSDs at $r/R = 1$, $r/R = 0.75$ and $r/R = 0.25$ for the lowest and the highest dissolution pressure, namely, 220 kPa and 500 kPa. Mean bubble sizes $d_{1,0}$ are displayed at the inset table for easier comparison. For the case of 220 kPa, BSDs and mean bubble sizes appear akin at the three radial positions. Thus, bubbles of all sizes are homogeneously spread across the column. On the contrary, at 500 kPa, although the peak for both small and large bubbles remains at the same bubble diameter for the two radial positions, the frequency of large bubbles increases compared to that of small bubbles at $r/R = 0.75$. The fact that under 500 kPa bubbles sizes near the wall are different than across the rest of the column is further indicated by the diverging mean diameters. The tendency of large bubbles to flow close to the column center is attributed to the action of Saffman lift force [33]. BSDs at different radial positions for the other dissolution pressures are not displayed in the plot due to large concentration of data. However, it is worthy to report that bubbles radial dispersion under 300 kPa follows the trend of 220 kPa, whereas that of 400 kPa resembles 500 kPa. As far as we know, this is the first time that radial bubble size variation across a degassing column is studied during flow decompression.

As radial bubble size homogeneity is not valid for every dissolution pressure, the effect of dissolution pressure on bubble size is presented separately for each radial position. Fig. 8a and b show the obtained BSDs under the examined dissolution pressures at $r/R = 1$ and $r/R = 0.75$ respectively. Mean diameters and standard deviation values are included at the inset table. For the unimodal BSDs at 220 kPa and 300 kPa there are unique mean and standard deviation values. Yet, for the bimodal BSDs at 400 kPa and 500 kPa there are two mean and standard deviation values, one for microbubbles and one for macrobubbles. Mean bubble diameter for 220 kPa is 266 μm . According to Fig. 8a and b, increasing the dissolution pressure from 220 kPa to 300 kPa triggers the formation of microbubbles during degassing. The size of microbubbles remains the same at higher dissolution pressures. What really changes in case of 400 kPa and 500 kPa is the formation of macrobubbles co-existing with microbubbles within the flow. The fraction of macrobubbles increases with pressure and radial distance from the column wall. Even though the range of bubble radius in the reported bubble size distributions stops at 800 μm there are still a few bubbles overcoming that size, the contribution of which, however, in the number probability densities of Figs. 7 and 8 is negligible.

Mean diameters at 220 kPa (Fig. 8a and b) are completely out of

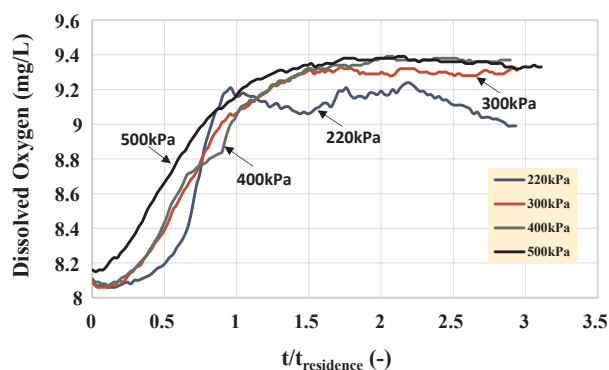


Fig. 5. Concentration of oxygen dissolved in the liquid stream exiting the column at $z/D = 22.5$, under various dissolution pressures.

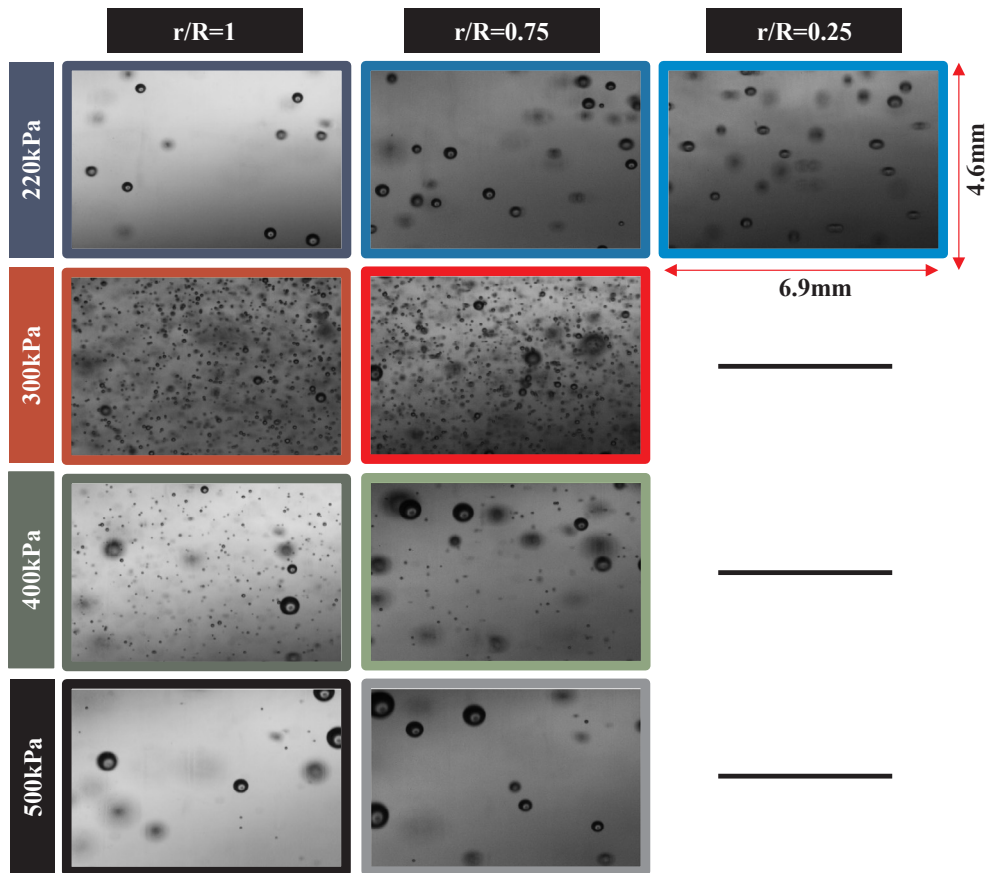


Fig. 6. Bubble images at $r/R = 1$, $r/R = 0.75$ and $r/R = 0.25$ under 220 kPa, 300 kPa, 400 kPa and 500 kPa dissolution pressures.

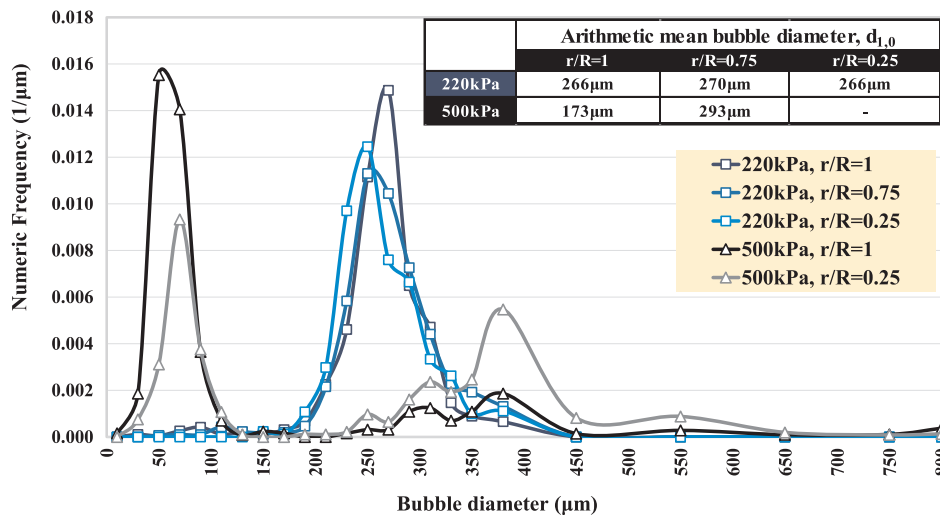


Fig. 7. Bubble size distributions at $r/R = 1$, $r/R = 0.75$ and $r/R = 0.25$ for 220 kPa and 500 kPa.

range regarding the results of relative DAF works which vary between 30 and 70 μm for operating pressures of 200–600 kPa [7,15,17,23,25]. However, the range of microbubbles obtained at higher dissolution pressures fit nicely with the above results, albeit the presence of macrobubbles which renders the overall mean diameters at 400 kPa and 500 kPa significantly larger. It must be noted that in some previous works, macrobubbles could not even be detected by the employed optical techniques [19,24,25].

The presence of macrobubbles in DAF is mentioned also by other researchers. Rykaart and Haarhoff [7] set the limit to 150 μm (diameter value) above which bubbles are considered as macrobubbles. Based on

this critical diameter, they showed that the fraction of macrobubbles increases with dissolution pressure. Their conclusion is valid also in the present work, excluding the case of 220 kPa where macrobubbles fraction approaches 100%. Rykaart and Haarhoff [7] attributed the formation of macrobubbles to coalescence due to both large concentrations of bubbles and large eddies in the flow. Ponasse et al. [18] set the macrobubbles limit diameter to 500 μm and reported their presence when saturated water was released from 400 kPa to the atmosphere. Formation of macrobubbles was attributed again to coalescence, although this time due to the weak hydrodynamic turbulence away from the nozzle. Apparently, if DAF application is of concern the

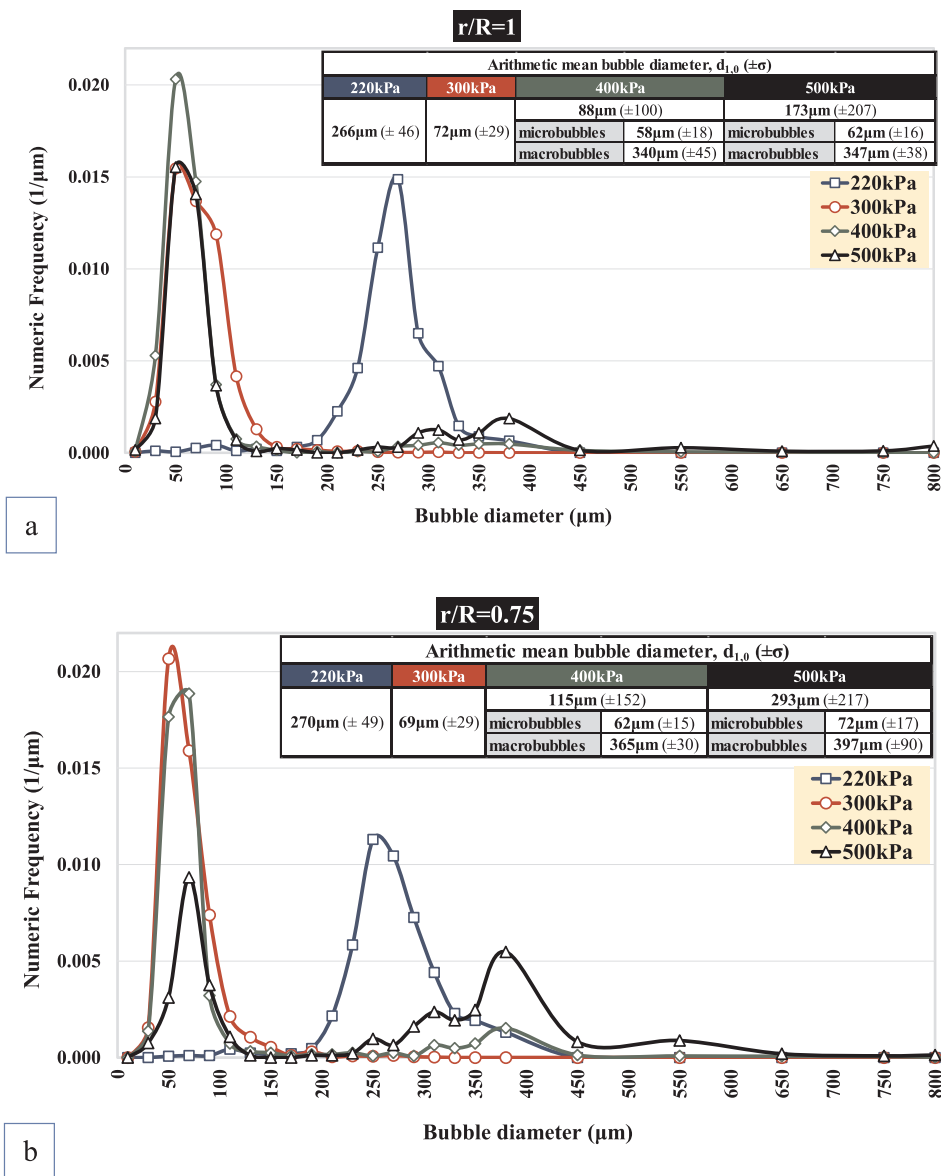


Fig. 8. Bubble Size Distributions under various dissolution pressures, (a) at $r/R = 1$ and (b) at $r/R = 0.75$.

present study suggests that in the employed geometry of the column a dissolution pressure close to 300 kPa is advantageous since the fraction of macrobubbles is minimum.

3.4. Volumetric gas fraction

Fig. 9 displays an indicative gas fraction (ϵ) evolution curve at $z/D = 22.5$ during the decompression degassing of a liquid jet saturated at 300 kPa. At the beginning of injection, only liquid flows between the ring electrodes at $z/D = 22.5$ and thus the gas fraction is zero. As time proceeds, more desorbed gas rises to the electrodes, and as a result the gas fraction increases until it reaches steady state.

Fig. 10 presents mean gas fraction (ϵ) values at $z/D = 22.5$ generated due to the decompression of a liquid saturated at 220 kPa, 300 kPa, 400 kPa and 500 kPa. The error bars show the standard deviation of several repetitions under the same experimental conditions. Based on Henry's law, one would expect the desorbed gas fraction to increase linearly with dissolution pressure as the excess dissolved gas is proportional to the level of decompression. The only exception to this linear behavior is the low mean gas fraction value measured at under 500 kPa. According to the optical results presented above (Fig. 8), the

frequency of macrobubbles generation becomes significant under 500 kPa dissolution pressure. High buoyancy velocities of these

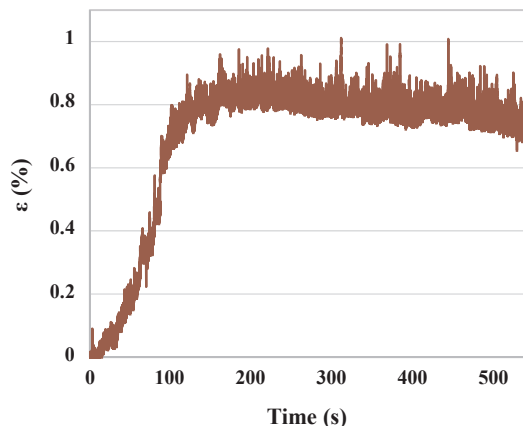


Fig. 9. Gas fraction (ϵ) time evolution during the whole injection under 300 kPa dissolution pressure, at $z/D = 22.5$.

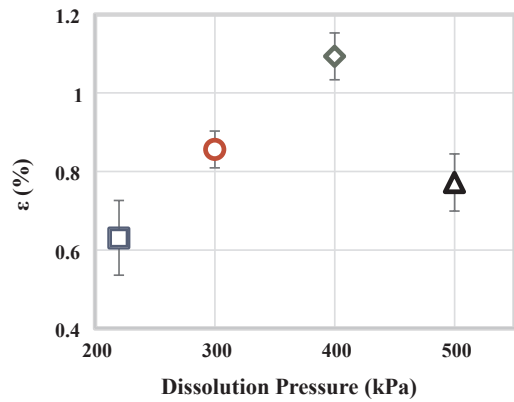


Fig. 10. Mean gas fraction (ϵ) at various dissolution pressures.

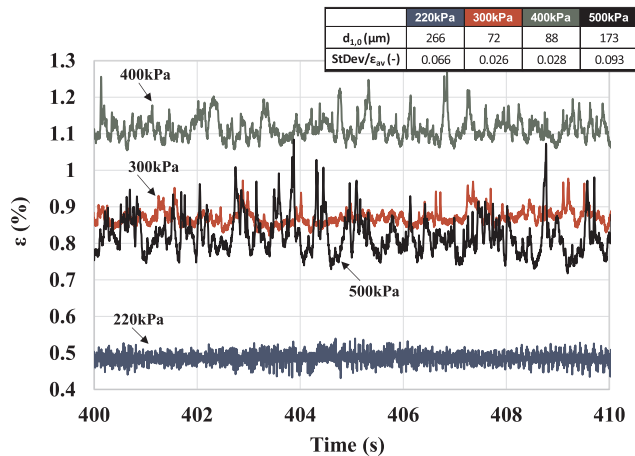


Fig. 11. Gas fraction (ϵ) fluctuations with time under several dissolution pressures.

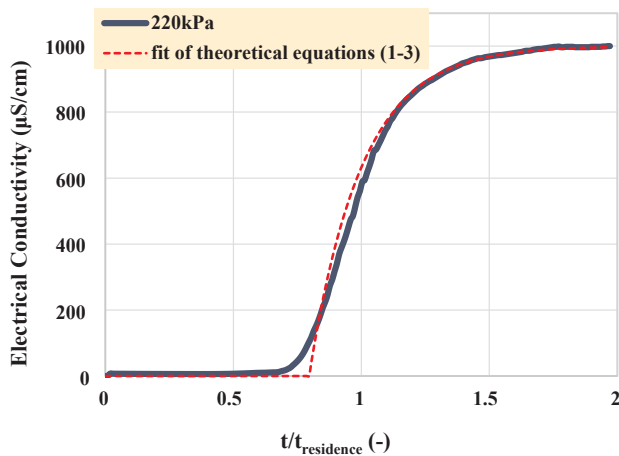


Fig. 12. Fitting residence time distribution curve of 220 kPa with theoretical exponential equation.

macrobubbles restrict their residence time inside the column and therefore reduce the gas fraction [34].

Fig. 11 shows the fluctuations of gas fraction (ϵ) measurements during a time series of only 10 s for every examined dissolution pressure. These 10 s period is selected to start 400 s after injection, so as to be part of the steady state region for all dissolution pressures. As Kostoglou [35] suggested theoretically and Evgenidis and Karapantsios [29] confirmed experimentally, the ratio of the gas fraction standard deviation (StDev) over the gas fraction mean value (ϵ_{av}) is proportional to the average bubble size. The same is seen here, too, since larger

average bubble sizes are associated with larger $\text{StDev}/\epsilon_{av}$ values. This not only confirms the present optical bubble size data but also shows that arguments made over discrete optical snapshots are valid continually during the degassing period.

4. Discussion

The process presented here is very complicated incorporating several sub-processes (i.e. complex flow and dissolved gas concentration fields combined with bubble nucleation, growth and coalescence). The above constitutes a far more complicated case than the existing knowledge on conventional bubble columns (where bubbles are simply introduced and not gradually created inside the flow field) and as a result its direct modeling is prohibitively complicated. In addition, the flow field is much more intense than those met in bubble columns. It is noted that a jet like the present one becomes unstable at a Reynolds number around 50 [36]. Here the Reynolds number is of the order of several thousands (see Table 1) rendering necessary the use of turbulence models and thus introducing uncertainty to the modeling process [37]. The existence of bubbles further complicates the flow field. So the choice here is to use mixing models to empirically model the flow field based on the experimental residence time distributions. The measured gas fraction is always much less than 10% so a one way coupling between liquid and gas flow can be approximately assumed. Therefore, only the liquid residence time distributions will be used to extract the mixing model.

Initially a generalized dispersion model is considered to model the flow [38]. The high shear created by the decelerating liquid jet combined to the zero wall velocity leads to strong recirculation (and thus high mixing) at the jet region. The jet decelerates along the flow and eventually vanishes to a simple laminar flow (small mixing). The above view is confirmed by visual observations in S1 Video. Turbulent flow at the bottom of the column is indicated by the chaotic bubbles trajectory. Flow turns to laminar as it moves to the top, thus bubbles follow a smoother vertical path towards the liquid free surface. So, a decreasing dispersion coefficient is expected from the bottom to the top of the column. Attempts to fit the experimental residence time distribution showed that the data could be approximately described by a very large dispersion coefficient up to a specific column height and by a zero dispersion coefficient for the rest of the column. This behavior permits the approximation of the generalized mixing model with a much simpler one: perfect mixing up to a height $z = L_1$ and no mixing from $z = L_1$ to bubble column top $z = L$. The only fitting parameter is the value of L_1 . The particular model leads to the following equations for the residence time distribution $EC(t/t_{residence})$ (Fig. 4).

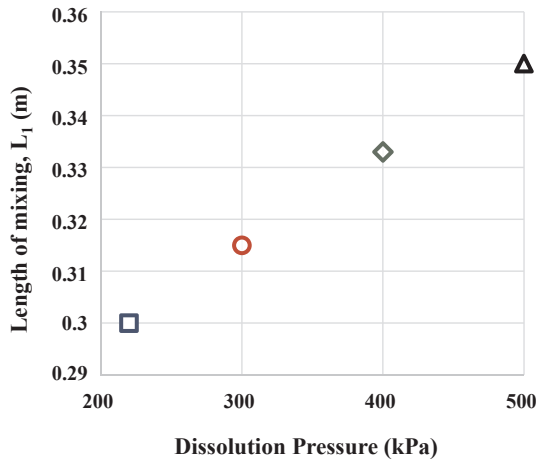


Fig. 13. Complete mixing column length, varying with dissolution pressure.

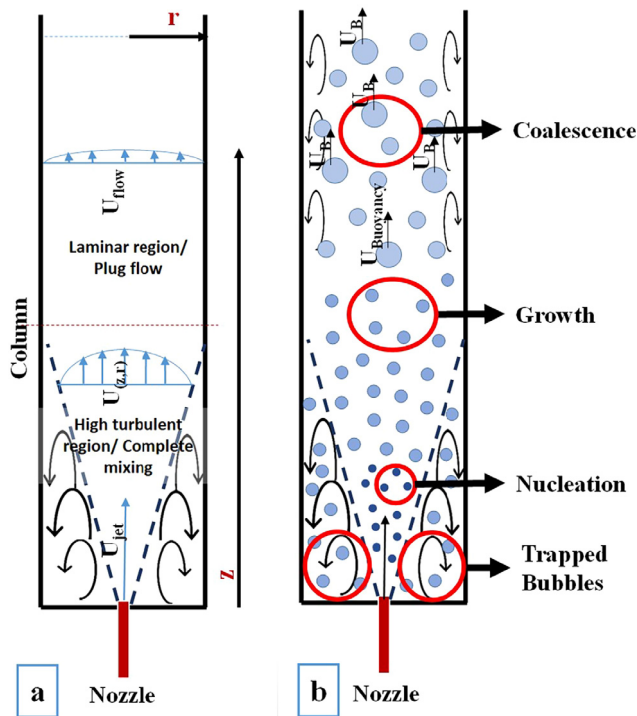


Fig. 14. Schematic description of, (a) Jet dispersion in the column and (b) Bubble formation and growth.



S1 Video.

$$EC\left(\frac{t}{t_{residence}}\right) = 0, \text{ for } t < t_2 \tag{1}$$

$$EC\left(\frac{t}{t_{residence}}\right) = 1000 \times \left[1 - \exp\left(-\frac{t-t_2}{t_1}\right)\right], \text{ for } t \geq t_2 \tag{2}$$

where,

$$t_{residence} = t_2 + t_1 \text{ and } t_1 = \frac{L_1}{L} \times t_{residence} \tag{3}$$

The residence time of the liquid in the mixing zone of the column is t_1 , while t_2 denotes liquid residence time in the plug flow zone. A typical fit of the above equations to the 220 kPa data is shown in Fig. 12. It is noted that the smooth uprising behavior of data at the region $t = t_1$ rather does not reflect a gradually increasing dispersion at the upper part of the column but it is completely explained by the way of obtaining the experimental curve, i.e., by measuring conductance in a small mixing vessel outside the column (Overflow Vessel, Fig. 1) which is equivalent to apply a smoothing operator to the mixing model equation. The value of the length L_1 as a function of the liquid dissolution pressure is presented in Fig. 13. It is apparent that the length of the completely mixed region increases slightly as the pressure (and thus the jet flow rate) increases.

Having approximately described the liquid flow field in the column it is useful now to discuss the phenomena related to the appearance of bubbles. At first, supersaturation leads to bubble nucleation. The critical nucleus size can be easily assessed from the Young-Laplace equation $R_c = 2\gamma/S$ where γ is the surface tension, S is the supersaturation parameter defined as $S = (C/C_{eq}) - 1$ (C is the gas concentration in liquid and C_{eq} the corresponding gas solubility). A simple calculation shows that R_c here is of the order of micrometers indicating that the nucleation processes is not influenced by the turbulence. The nucleation

rate is in general a strong function of supersaturation. There is no meaning in attempting to compute characteristic nucleation times since it is well known that the theory is too far from reality [39]. Bubbles smaller than R_c disappear whereas those larger than R_c grow. Bubble growth due to degassing for bubbles larger than $20\ \mu\text{m}$ is dominated by mass transfer [5]. So, bubbles start growing under the combined effect of diffusion and convection, due to the flow field created by bubble growth itself. The relative significance of the two phenomena are indicated by the so called foaming number $F_m = (\text{gas excess concentration in the liquid})/(\text{gas density})$ [5]. The Foaming number in the present work never exceeds the value 0.1 (being much less in most of the cases) indicating that the growth can be assumed to occur solely by diffusion (i.e. quasi-steady conditions). As a bubble grows it starts to accelerate due to buoyancy. Its increasing velocity creates a convection contribution to mass transfer. In other words, the diffusional growth increases bubble size leading to relative motion between bubble and liquid, therefore, increasing further the mass transfer by convection. Two other phenomena affecting also bubble size are breakage and coalescence. Bubble breakage does not occur in the present system, as the size of bubbles is considerably small in the jet region (high turbulent intensity) whereas at the region of larger bubbles the turbulent intensity is almost zero [40]. On the contrary, there are two sources of coalescence in the present case. The first refers mainly to smaller bubbles and it has to do with turbulent velocity fluctuations/gradients. The second refers to larger bubbles and it has to do with different buoyancy velocities among the bubbles. A further complication arises from the different velocities between the liquid and gas phase due to buoyancy. Adopting a very simple two phase flow model, the continuity equation for the gas (ignoring bubble growth) leads to $U_{\text{bubbles}}\varepsilon = K$ along the flow, where ε is the gas fraction and K is a constant. This implies that the gas fraction is $\varepsilon = K/(U_{\text{flow}} + U_{\text{buoyancy}})$ which means that for a fixed dissolved gas concentration the gas fraction is inversely proportional to bubble velocity and thus is directly affected by bubble size.

The sequence of phenomena occurring in the column may be as follows. The liquid flow field starting from a high mixing region (surrounding the incoming jet) at the bottom and ending to a laminar flow region a bit higher (actually above L_j) is shown in Fig. 14a. Bubbles nucleate in the jet region and get trapped in the high mixing region where apart from growth they may also undergo turbulent coalescence (Fig. 14b). These phenomena may continue up to the first part of the low mixing region. Latter in this region the only phenomenon occurring is gravity driven coalescence. The dominant phenomena in each region according to the above scenario are shown in Fig. 14a, b. At this point, selection of $z/D = 22.5$ height for measurement execution can be justified. Fig. 14b shows that $z/D = 22.5$ belongs to the zone of gravitational coalescence. This means that at $z/D = 22.5$ supersaturation has diminished (Fig. 5) and so bubbles are not expected to grow further in size. Furthermore, $z/D = 22.5$ belongs to the plug flow region (Fig. 13) where no flow instabilities are expected. This can be also optically witnessed in S1 Video, as smooth vertical trajectory of bubbles passes from the measuring point. Measuring above $z/D = 22.5$ would intensify the impact of gravitational coalescence on bubble size, resulting in BSDs that diverge from those attributed to the desorption of gas.

Experimental findings of the present work are explained below. In the case of lower liquid pressurization, the supersaturation is small leading to low nucleation rate, small number of nuclei and thus to larger bubble sizes at the end of degassing. In addition, gravitational coalescence appears to contribute to the relative narrow size distribution. Smaller bubbles merge with larger ones narrowing the size distribution resulting from the well-mixed region. The nucleation rate is larger in the case of 300 kPa pressure leading to a larger number of nuclei and thus of a smaller final bubble size (nucleation rate increases non-linearly with supersaturation whereas dissolved gas concentration increases linearly). Gravitational coalescence is insignificant in this case due to the much smaller size of bubbles. The situation changes

somewhat for larger pressures. The slightly extended mixing length (see Fig. 13) combined to nucleation and growth rates may also contribute to broadening of the BSDs. The macrobubbles of the tail in these distributions are destabilized and leave the mixing area due to buoyancy. Then, as they rise they scavenge the small bubbles that they encounter in their trajectory increasing considerably their size (and leading to the second mode in the corresponding BSDs). Such behavior is compatible with the almost similar shapes of the narrow BSDs for 400 kPa and 500 kPa, and the somewhat broader shape for 300 kPa. The population of macrobubbles increases as the pressure increases from 400 kPa to 500 kPa. The above scenario for large bubbles creation is confirmed by the corresponding video for the 500 kPa (S1 Video) which clearly shows that at the top of the column large bubbles have merged with most small ones. In general the problem at hand is a very complex one and the above discussion gave only a first physical explanation to some of the observed phenomena. A complete understanding of the process requires additional experiments having isolated the effects of different parameters (measuring locations, dissolution pressures, injection velocities) and quantitative description of the phenomena.

5. Conclusions

The present work investigates the effect of dissolution pressure on the final size of gas bubbles formed when a pressurized water jet saturated with dissolved gas is injected through a nozzle to a column of low pressure stagnant water. For that purpose, a flow decompression degassing experimental setup is constructed. Four different dissolution pressures are employed (220 kPa, 300 kPa, 400 kPa and 500 kPa). Dissolved oxygen measurements in the liquid overflowing stream confirm completeness of gas desorption. It is shown that under 220 kPa dissolution pressure, larger bubbles are formed as the desorbed gas is distributed in a much lower number of nuclei. The size distribution obtained is narrow as the mixing zone becomes more constricted under low dissolution pressures. The slightly extended mixing length under higher dissolution pressures (400 kPa and 500 kPa) leads to the broadening of bubble size distributions. In addition, larger bubbles grow more in size due to gravitational coalescence, resulting in bimodal size distributions. Therefore, the narrow bubble size distribution with an average size of $70\ \mu\text{m}$ obtained under 300 kPa, makes this working pressure the optimum one in terms of Dissolved Air Flotation application, regarding the geometry of the present degassing setup.

Acknowledgements

This study is funded by  (NPI Project: Bubble dynamics during degassing of liquids – Contract No.: 4000108790/13/NL/PA) and carried out under the umbrella of COST Action MP1106: ‘Smart and green interfaces – from single bubbles and drops to industrial, environmental and biomedical applications’ and COST Action MP1305: ‘Flowing matter’. We wish to thank Dr. Christian Schwarz, Technical Officer of ESA NPI Project (Contract No.: 4000108790/13/NL/PA) ‘Bubble dynamics during degassing of liquids’, for his useful comments on the original manuscript. The view expressed herein can in no way be taken to reflect the official opinion of the European Space Agency.

References

- [1] L.E. Scriven, On the dynamics of phase growth, *Chem. Eng. Sci.* 10 (1958) 1–13.
- [2] C.E. Brennen, *Cavitation and Bubble Dynamics*, Oxford University Press, Oxford, 1995.
- [3] Y. Maeda, S. Hosokawa, Y. Baba, A. Tomiyama, Y. Ito, Generation mechanism of micro-bubbles in a pressurized dissolution method, *Exp. Therm Fluid Sci.* 60 (2015) 201–207.
- [4] Y. Gu, B. Li, M. Chen, An experimental study on the cavitation of water with effects of SiO_2 nanoparticles, *Exp. Therm Fluid Sci.* 79 (2016) 195–201.
- [5] M. Kostoglou, T.D. Karapantsios, Bubble dynamics during the non-isothermal degassing of liquids. exploiting microgravity conditions, *Adv. Colloid Interface Sci.* 134–135 (2007) 125–137.

- [16] A. Cioncolini, L. Santini, M.E. Ricotti, Effects of dissolved air on subcooled and saturated flow boiling of water in a small diameter tube at low pressure, *Exp. Therm. Fluid Sci.* 32 (2007) 38–51.
- [7] E.M. Rykaart, J. Haarhof, Behaviour of air injection nozzles in dissolved air flotation, *Water Sci. Technol.* 31 (3–4) (1995) 25–35.
- [8] Y.M. Chen, S.C. Wu, C.I. Chu, Thermal performance of sintered miniature heat pipes, *Heat Mass Transfer.* 37 (2001) 611–616.
- [9] K. Sathyan, H.Y. Hsu, S.H. Lee, K. Gopinath, Long-term lubrication of momentum wheels used in spacecrafts—an overview, *Tribol. Int.* 43 (2010) 259.
- [10] R.G. Cunningham, A.G. Hansen, T.Y. Na, Jet pump cavitation, *J. Basic Eng.* 92 (3) (1970) 483–492.
- [11] R.W. Mitchell, The Forties field sea-water injection system, *J. Pet. Technol.* 30 (6) (1978) 877–884.
- [12] J. Conkin, Evidence-based approach to the analysis of serious decompression sickness with application to EVA astronauts. NASA-TP-2001-210196, 2001.
- [13] J.K. Edzwald, Developments of high rate dissolved air flotation for drinking water treatment, *J. Water Supply Res. T.* 56 (2007) 399.
- [14] Z. Huang, S. Yiming, S. Shiga, H. Nakamura, T. Karasawa, T. Nagasaka, Atomization behavior of fuel containing dissolved gas, *Atomiz. Sprays.* 4 (3) (1994) 253–262.
- [15] S.E. Burns, S. Yiacoumi, C. Tsouris, Microbubble generation for environmental and industrial separations, *Sep. Purif. Technol.* 11 (1997) 221–232.
- [16] A.G. Vlyssides, S.T. Mai, E.P. Barampouti, Bubble size distribution formed by depressurizing air-saturated water, *Ind. Eng. Chem. Res.* 43 (11) (2004) 2775–2780.
- [17] T. Takahashi, T. Miyahara, H. Mochizuki, Fundamental study of bubble formation, *J. Chem. Eng. Jpn.* 12 (4) (1979) 275–280.
- [18] M. Ponasse, V. Dupre, Y. Aurelle, A. Secq, Bubble formation by water release in nozzle II: influence of various parameters on bubble size, *Water Res.* 32 (8) (1998) 2498–2506.
- [19] S.E. De Rijk, J.G. den Blanken, Bubble size in flotation thickening, *Wat. Res.* 28 (2) (1994) 465–473.
- [20] H.J.B. Couto, D.G. Nunes, R. Neumann, S.C.A. Franca, Micro-bubbles size distribution measurements by laser diffraction technique, *Miner. Eng.* 22 (2009) 330–335.
- [21] C.T. O'Connor, E.W. Randall, C.M. Goodall, Measurement of the effects of physical and chemical variables on bubble size, *Int. J. Miner. Process.* 28 (1990) 139–149.
- [22] A. Cubeddu, C. Rauh, V. Ulrich, Simulations of bubble growth and interaction in high viscous fluids using the lattice Boltzmann method, *Int. J. Multiph. Flow* 93 (2017) 108–114.
- [23] F. Chen, F. Peng, X. Wu, Z. Luan, Bubble performance of a novel dissolved air flotation (DAF) unit, *J. Environ. Sci.* 16 (1) (2004) 104–107.
- [24] S. Hosokawa, K. Tanaka, A. Tomiyama, Y. Maeda, S. Yamaguchi, Y. Ito, Measurement of micro bubbles generated by a pressurized dissolution method, *J. Phys.* 147 (2009) 1–10.
- [25] R.T. Rodrigues, J. Rubio, New basis for measuring the size distribution of bubbles, *Miner. Eng.* 16 (2003) 757–765.
- [26] G.J. Schers, J.C. Van Dijk, 1992. Chemical water and treatment II, in: *Dissolved-Air Flotation: Theory and practice*. 5th Gothenburg Symposium. France, pp. 223–246.
- [27] X. Zabulis, M. Papara, A. Chatziargyriou, T.D. Karapantsios, Detection of densely dispersed spherical bubbles in digital images based on a template matching technique: application to wet foams, *Colloids Surf. A: Physicochem. Eng. Aspects* 309 (2007) 96–106.
- [28] T.D. Karapantsios, S.P. Evgenidis, K. Zacharias, T. Mesimeris, Method for the detection and characterization of bubbles in liquids and device therefor, resp. system, European Patent Office, Application Number EP14188200.1, 2014.
- [29] S. Evgenidis, T. Karapantsios, Effect of bubble size on void fraction fluctuations in dispersed bubble flows, *Int. J. Multiph. Flow.* 75 (2015) 163–173.
- [30] W.D. Deckwer, *Bubble Column Reactors*, Wiley, New York, 1992.
- [31] W.T. Shannon, D.H. Buisson, Dissolved air flotation in hot water, *Water Res.* 14 (1980) 759–765.
- [32] H. Kikukawa, Physical and transport properties governing bubble column operations, *Int. J. Multiph. Flow* 93 (2017) 115–129.
- [33] C.T. Crowe, M. Sommerfeld, Y. Tsuji, *Multiphase Flows with Droplets and Particles*, CRC Press, Boca Raton, 1998.
- [34] S.S. Alves, S.P. Orvalho, J.M.T. Vasconcelos, Effect of bubble contamination on rise velocity and mass transfer, *Chem. Eng. Sci.* 60 (2005) 1–9.
- [35] M. Kostoglou, On the effect of flowing circular entities swarms on strip electrodes conductance, *Ind. Eng. Chem. Res.* 51 (2012) 5615–5625.
- [36] J. Horwitz, S. Rosenblat, Nonlinear stability of a viscous axisymmetric jet, *Acta Mech.* 95 (1) (1992) 131–156.
- [37] J. Mathieu, J. Scott, *An Introduction to Turbulent Flow*, Cambridge University Press, London, 2000.
- [38] E.B. Nauman, B.A. Buffham, *Mixing in Continuous Flow Systems*, Wiley, New York, 1983.
- [39] S.D. Lubetkin, Why is it much easier to nucleate gas bubbles than theory predicts? *Langmuir* 19 (7) (2003) 2575–2587.
- [40] M. Kostoglou, A.J. Karabelas, Towards a unified framework for the derivation of breakage functions based on the statistical theory of turbulence, *Chem. Eng. Sci.* 60 (2005) 6584–6595.